Statistical description of matched field processing ambiguity surfaces

Brian H. Tracey and , and

Citation: The Journal of the Acoustical Society of America **118**, 1372 (2005); doi: 10.1121/1.2000750
View online: http://dx.doi.org/10.1121/1.2000750
View Table of Contents: http://asa.scitation.org/toc/jas/118/3
Published by the Acoustical Society of America

Statistical description of matched field processing ambiguity surfaces

Brian H. Tracey
MIT Lincoln Laboratory, 244 Wood Street, Lexington, Massachusetts 02420

(Received 6 November 2004; revised 16 June 2005; accepted 17 June 2005)

The relationship between array design and ambiguity surface characteristics is not straightforward for matched field processing (MFP). Because MFP makes use of multipath propagation, ambiguities are a function of the environment as well as the array. This paper develops a statistical approach that seeks to provide an analytic link between array design and metrics describing the MFP output. Approximate expressions are derived for the probability distribution of power output across conventional MFP ambiguity surfaces. The validity of the expressions is examined through numerical simulation. This approach can be used as a design tool for comparing the expected performance of different array geometries. © *2005 Acoustical Society of America.* [DOI: 10.1121/1.2000750]

PACS number(s): 43.30.Wi, 43.60.Fg, 43.60.Uv [EJS] Pages: 1372–1380

I. INTRODUCTION

For plane-wave and range-focused beamforming, the relationship between array geometry and the array response is well understood.[1] Quantities such as array resolution and sidelobe levels can be calculated in a straightforward manner. A set of similar guidelines linking the array geometry to array response does not currently exist for matched field processing (MFP). MFP uses full-field propagation models to account for multipath when constructing steering vectors for beamforming.[2] A major difficulty in deriving guidelines is that the array response depends on the environment for MFP. Thus array design for MFP is often studied through numerical simulations. While these studies can be of significant value, analytic tools for array design are also desirable.

Since MFP seeks to exploit multipath, an ideal receive array would provide orthogonal sampling of the propagating normal modes. For a vertical line array (VLA), this means that the array should span as much of the water column as possible, with depth sampling sufficient for sampling the highest trapped mode.[3,4] Horizontal line arrays (HLAs) rely on mode orthogonality in the range dimension to separate the propagating modes, leading to requirements on array length.[5,6] The mode correlation matrix (MCM), which describes cross-talk between modes, provides a useful way to characterize an array's ability to resolve multipath. HLA and VLA geometries can be directly compared using metrics that describe the extent to which the MCM is diagonally dominant.[7,8]

MFP ambiguity surfaces are characterized by a complicated set of local maxima and minima that shift with source location and environmental parameters. As a result, they have often been described by statistical measures such as peak-to-average sidelobe ratio and deflection index.[9] The approach taken in several previous studies of MFP array design[7,8] is to simulate MFP output for different arrays, calculate statistics describing the ambiguity surfaces, and correlate these statistical measures with metrics describing the diagonality of the mode correlation matrix. In contrast, the work below seeks to develop an *analytic* link between mode resolution and a statistical description of the MFP ambiguity surface. The analytic approach can help give additional insight into the array design problem. The results below show how ambiguity surface statistics depend on the mode shapes and attenuations across the ranges and depth searched, in addition to the mode correlation matrix.

The first two sections below show the MFP ambiguity structure for several example arrays and present an expression relating the conventional MFP (CMFP) output to the mode correlation matrix. The following sections derive the predicted sidelobe distribution for narrow-band and broadband CMFP. Monte Carlo simulations are then used to explore the accuracy of the predictions as a function of array geometry. Criteria are developed to identify when good quantitative agreement can be expected. Examples below also suggest that the analytic approach can provide better qualitative ranking of array performance than commonly used metrics such as MCM diagonality.

II. DEPENDENCE ON ARRAY GEOMETRY

As motivation, the effects of array geometry on MFP are examined for a representative shallow water environment. Simulations were generated based on environmental data gathered for the Santa Barbara channel experiment (SBCX).[10] This environment consists of a 209-m-deep water column with a downward refracting sound speed profile, as shown in Fig. 1. The seabed in the SBCX site was described as a series of sediment layers, with properties given in Table I. The KRAKEN normal mode model[11] was used for the simulations, with the environment assumed to be range independent.

Simulations were carried out for four array geometries. Properties of the arrays are listed in Table II. The first array geometry was a vertical line array (VLA) spanning 80% of the water column. This array span is similar to those actually used during the SBCX data collection. A second VLA was modeled that spanned only 40% of the water column. Two

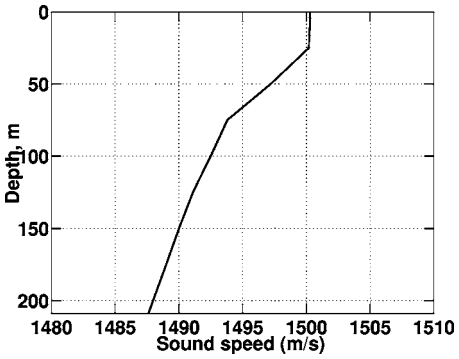

FIG. 1. Sound speed profile used for simulations, taken from SBCX measurements.

horizontal line arrays (HLAs), of 1 km and 500 m length respectively, were modeled. Both HLAs were oriented at endfire to the source, as multipath resolution and MFP performance are best for HLAs at this orientation. Narrow-band simulations were done for a frequency of 120 Hz. This frequency is in the range of projected tones used in SBCX and other MFP experiments.

Conventional, or Bartlett, MFP surfaces were generated to demonstrate the localization possible with each array. No environmental mismatch was introduced. The signal was normalized so that the peak of the ambiguity surface equaled one. The conventional MFP output power is given by

$$b(\Theta) = \left| \frac{\mathbf{p}^H_{\text{look}}(\Theta)}{|\mathbf{p}_{\text{look}}(\Theta)|} \cdot \frac{\mathbf{x}(\Theta_S)}{|\mathbf{x}(\Theta_S)|} \right|^2, \tag{1}$$

where $\Theta=(r,z,\theta)$ is the MFP steering direction in three dimensions, Θ_S is the source location, $\mathbf{x}$ is the data, and $\mathbf{p}_{\text{look}}$ is the predicted pressure field on the array. The vector $\mathbf{p}_{\text{look}}$ and its normalization are kept separate, rather than being combined into a replica vector $\mathbf{v}$, for use in calculations below. In the absence of mismatch, the data vector $\mathbf{x}$ is a scaled version of the replica vector at the source location.

Simulated CMFP surfaces are shown in Fig. 2. The simulated noise source was located at 70-m depth and at 10-km range from the center of the receiver array. The 80% spanning VLA provides a good localization of the source. Significant ambiguities exist for the other arrays.

While the two HLAs clearly have high sidelobes, two points are worth noting. First, the horizontal aperture provides azimuthal discrimination that is not available with the VLAs. If only a single source is present along each bearing, it may be possible to track the MFP output over time to localize the source even though an instantaneous MFP output is highly ambiguous. Adaptive beamforming and broadband processing can also help to reduce ambiguities.

The HLA simulations also show that sidelobe levels are lower near the surface than at depth. This results from a combination of two effects. First, the HLAs can better resolve the high-angle modes associated with surface sources, as these arrive at conical angles closer to broadside. Second, the downward-refracting sound speed profile traps the lowest-order modes at depth.

TABLE I. Parameters for geoacoustic model of SBCX test site: z=depth from surface; c_c=compressional sound speed; ρ=density; α_c =compressional wave attenuation.

z (m)	c_c (m/s)	ρ (g/cm^3)	α_c (dB/λ)
209	1607	1.95	0.37
309	1702	1.95	0.37
309	1862	1.98	0.035
609	2374	1.98	0.035
609	2374	2.03	0.04

TABLE II. Parameters for arrays used in simulations. For vertical arrays, "depth" refers to the bottommost hydrophone in the array.

Type	No. of sensors	Spacing (m)	Length (m)	Depth (m)
80% VLA	50	3.4	166.6	208
40% VLA	50	1.7	83.3	208
1 km HLA	201	5	500	100
500 m HLA	101	5	1000	100

III. MODE CORRELATION MATRIX AND MFP OUTPUT

In this section the mode correlation matrix is defined and its link to the output of a Bartlett processor is shown. The acoustic source is assumed to be in the far field of an array of L sensors. The range r_i between each sensor and the source is given by

$$r_i = r_s + \Delta_i, \tag{2}$$

where r_s is the range from the source to the center of the array and Δ_i is the range increment to each sensor. For a perfectly straight VLA, $\Delta_i=0$ for all sensors. For a uniform straight HLA, $\Delta_i(\theta)=(x_i-x_{\text{ref}})\cos\theta$, where x is distance along the array and θ is bearing to the source. Using a normal mode description of the sound field, the pressure received on sensor i is given by

$$p(r_i,z_i,\theta) = \frac{i\sqrt{2\pi}e^{-i\pi/4}}{\sqrt{r_s}} \sum_n \frac{\psi_n(z_s)\psi_n(z_i)}{\sqrt{k_n}} e^{ik_n[r_s+\Delta_i(\theta)]}, \tag{3}$$

where ψ_n is the mode shape for mode n, k_n is the horizontal wave number for the mode, and z_s and z_i are the source depth and ith receiver depth, respectively. For matched field processing, replica vectors describing the response of the array to every possible source location are generated. Assuming that no mismatch exists, the replicas may be generated by using Eq. (3), evaluated for all look directions (r,z,θ).

For the far-field case, complex modal correlation matrices can be defined that include the range differences between elements, but not the absolute range:

$$e_{nm} = \sum_{i=1}^{L} \psi_n(z_i)\psi_m(z_i) e^{i(k_n\Delta_i(\theta_s)-k_m^*\Delta_i(\theta))}. \tag{4}$$

Since the modes are orthogonal, the mode correlation matrix will be diagonal for a fully spanning VLA.

This definition can be used to rewrite the CMFP output power given by Eq. (1). First, Eq. (3) is used to express the data vector $\mathbf{x}$, neglecting mismatch [mismatch can be in-

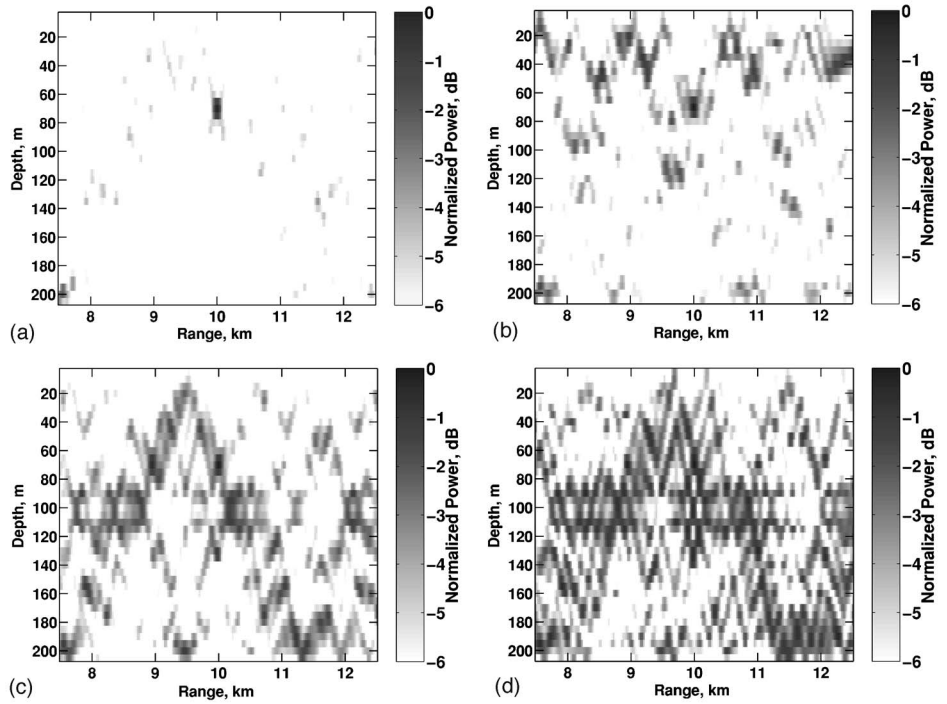

FIG. 2. Simulated CMFP ambiguity surfaces in the SBCX environment for the arrays considered. A 120-Hz source is located at 10-km range and 70-m depth, oriented at endfire to the horizontal arrays. Although HLAs have much higher sidelobes, they also have an ability to separate sources based on bearing that VLAs do not.

cluded by perturbing the modal horizontal wavenumbers in Eq. (3)]. All terms involving the array geometry are combined using the mode correlation in Eq. (4). The remaining terms may be grouped together, giving the output as

$$b(\Theta) = \left| \sum_{n,m} Y_{nm} e_{nm} \right|^2, \tag{5}$$

where Y_{nm} contains all information about the source location and look direction:

$$Y_{nm} = \frac{2\pi}{\sqrt{k_n k_m}} \frac{\psi_n(z_s)\psi_m(z) e^{i(k_n r_s - k_m^* r)}}{|\mathbf{p}_{\text{look}}(\Theta)||\mathbf{x}(\Theta_S)|}. \tag{6}$$

The conjugates on mode eigenvalues ensure that attenuation is handled correctly.

Before proceeding, it is helpful to study the mode correlation matrix in more detail. Figure 3 shows mode correlation matrices for the arrays defined in Sec. II. The plots are normalized so diagonal elements are equal to one. Modes 15 and higher have high loss and do not contribute to the acoustic field at long range. As expected, the 80% spanning VLA provides excellent resolution of the modal arrivals, while increased cross-talk is seen for the 40% VLA and the two HLAs.

A basic difference in the mode correlation patterns for vertical and horizontal arrays is seen in Fig. 3. For VLAs, the cross-talk between modes remains roughly similar as mode number increases, while for HLAs cross-talk decreases with mode order. The improved resolution of HLAs for higher modes results because higher modes impinge on the array at steeper vertical angles. These modes therefore arrive at conical angles that are closer to broadside, where the array resolution is better, and can be more easily separated.

While Fig. 3 shows results for endfire, Eq. (4) applies for any bearing angle. As the look direction bearing and source bearing diverge, the values of all components in the mode correlation matrix will drop. This reflects the filtering of source energy introduced by the conventional beampattern of the mode filter. Thus Eq. (4) and the results in the following sections can be used to determine the output power statistics as a function of the azimuthal difference from the source.

IV. NARROW-BAND CMFP STATISTICS

Equation (5) above expressed CMFP output power in terms of cross-modal correlations. That relationship is used here to derive approximate analytical results for the probability distribution of matched-field sidelobes. A statistical approach is based on the following assumptions.

(i) Statistics for the MFP surface are assembled by randomly sampling different MFP cells or "look directions." Thus the look direction can be treated as a random variable.
(ii) The true source location is unknown, so the source depth and range are assumed to be random variables.

The look direction depths are assumed to be distributed with uniform probability over depths $[D_{l1}, D_{l2}]$, while the source depths are distributed over $[D_{s1}, D_{s2}]$. Both source ranges and look direction ranges are assumed to be uniformly distributed over the full MFP search space, from R to $R+\Delta R$.

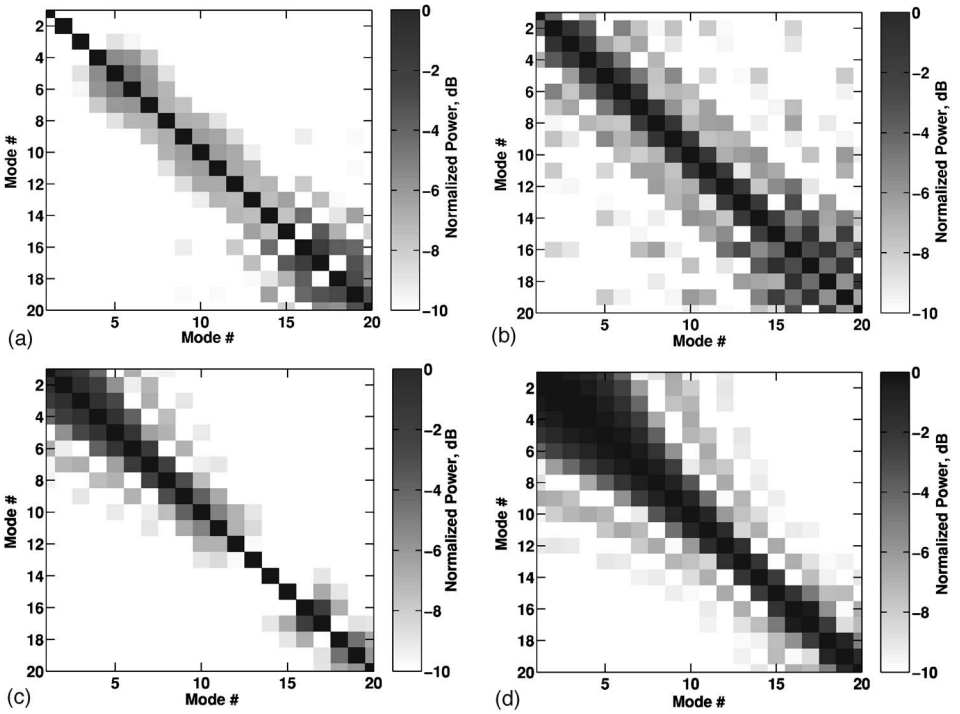

FIG. 3. Far-field mode correlation matrices for the arrays considered. Note the difference in structure between horizontal and vertical arrays.

Given the assumptions above, the terms Y_{nm} from Eq. (5) are zero-mean complex random variables (note that the mode correlation terms e_{nm}, which depend on array geometry, are considered deterministic). A further assumption is made that the random terms Y_{nm} are Gaussian distributed. Because many such terms are summed, inaccuracies in this assumption are reduced by the central limit theorem. The Y_{nm} are zero-mean, so only their variance needs to be calculated. The variance of the real part of Y_{nm} is found as (see the Appendix)

$$\sigma_{nm}^2 = \frac{2\pi^2}{k_n k_m} \int \frac{\psi_m^2(z)\psi_n^2(z_s)}{|\mathbf{p}_{\text{look}}(\Theta)|^2 |\mathbf{x}(\Theta_S)|^2} \times e^{-2\alpha_n r_s} e^{-2\alpha_m r} p_{\mathbf{r}}(\mathbf{r})\, d\mathbf{r}, \tag{7}$$

where $\mathbf{r}$ represents the independent random variables r_s, z_s, r, and z. A further assumption is required to represent the normalizing terms $|\mathbf{p}_{\text{look}}|^2$ and $|\mathbf{x}|^2$. For an array that resolves the modes well, off-diagonals will not contribute strongly to the intensity, and the norm-squared can be approximated by

$$|\mathbf{p}(\Theta)|^2 \approx \sum_{l=1}^{N_p} \frac{2\pi}{k_l} \psi_l^2(z) e_{ll} e^{-2\alpha_l r_{\text{mid}}}, \tag{8}$$

where N_p is the number of trapped (or proper) modes and r_{mid} is the mid-range of the MFP search region whose statistics are being calculated. This approximate normalization is discussed in more detail in the Appendix.

Numerical results below indicate that the assumption of a Gaussian distribution is reasonable. The approximation made in Eq. (8) appears to be a cause of inaccuracy for arrays with limited vertical aperture. Unfortunately, a more accurate (but analytically tractable) approximation has not been identified.

The Appendix shows that the assumptions above result in the following expression:

$$\sigma_{mn}^2 \approx \frac{4\pi^2}{2k_n k_m} Z_m(D_{l1}, D_{l2}) Z_n(D_{s1}, D_{s2}) \times R_m(R, \Delta R) R_n(R, \Delta R), \tag{9}$$

where Z_m and R_m account for depth and range integrations. The range integral R_m accounts for mode attenuation over the range of the ambiguity surface:

$$R_m(R, \Delta R) = \frac{e^{-2\alpha_m R}}{2\alpha_m \Delta R} [e^{-2\alpha_m \Delta R} - 1], \tag{10}$$

while the depth integrals are given by

$$Z_m(D_1, D_2) = \int_{D_1}^{D_2} \frac{\psi_m^2(z)dz}{\Delta D \sum_{l=1}^{N_p} (2\pi/k_l) \psi_l^2(z) e_{ll} e^{-2\alpha_l r_{\text{mid}}}}, \tag{11}$$

where D_1 and D_2 are the lower and upper depths of integration, and $\Delta D = D_2 - D_1$. Separate integrals over depth are required for the source and replicas, as the region of possible source depths can be different than the MFP search region.

Equation (9) gives the variance for the real part of a single Y_{nm} term from Eq. (5). These terms are multiplied by e_{nm} and summed to give another complex zero-mean Gaussian random variable, denoted Y. The variances of the real and imaginary parts of Y are equal and are given by

$$\sigma_Y^2 = \sum_{n,m} \sigma_{nm}^2 |e_{nm}|^2. \tag{12}$$

Finally, the absolute value-squared is taken as shown in Eq. (5), yielding an exponential probability distribution:

$$P_{NB}(b) = \frac{1}{\mu} e^{-b/\mu}, \tag{13}$$

where

$$\mu = 2\sum_{n,m} \sigma_{nm}^2 |e_{nm}|^2. \tag{14}$$

The interpretation of this result is that the ambiguity surface distribution is controlled by the amount of mode cross-talk, as measured by e_{nm}, weighted by a factor σ_{mn}^2 that captures the mode excitation and attenuation.

Equation (13) is an approximate result and can give nonphysical behavior (i.e., nonzero probability of $b>1$). A metric that describes its range of validity is therefore required. One useful approach is to require that the probability of nonphysical behavior is below a threshold; for example $\Pr(b>1)<0.01$. This metric is demonstrated in the numerical results below.

Several results can be found directly from Eq. (13). The percentage of the ambiguity surface that has a value higher than some threshold γ is given by

$$\Pr(b > \gamma) = e^{-\gamma/\mu}. \tag{15}$$

For example, the fraction of the surface within 3 dB of the peak is found by setting $\gamma=0.5$. Finally, the expected value of the exponential distribution is μ. This means that the average peak-to-sidelobe ratio, which has been used as a statistic for describing MFP ambiguity surfaces, is given by μ.

V. STATISTICS FOR INCOHERENT BROADBAND CMFP

When the source being localized has broadband energy, frequency averaging may be used to reduce ambiguities in the output. Frequency averaging is beneficial because the location of MFP ambiguities shifts over frequency while the true source location remains fixed. Thus high ambiguities at one frequency are averaged together with lower output at other frequencies. Linear averaging has been widely applied to MFP:[9,12]

$$I_{BB} = \frac{1}{M}\sum_{i=1}^{M} b(f_i). \tag{16}$$

Other options include averaging cross-frequency components[13] or averaging matched field outputs in decibels rather than in linear power.[14] Only linear averaging is analyzed here.

The results in Sec. IV can be used to find the PDF for broadband CMFP. In doing so, the assumption is made that the frequencies being averaged are spaced widely enough that their sidelobe locations can be treated as uncorrelated. Conditions for this to be true are discussed below. If more closely spaced frequencies are added, little benefit in terms of sidelobe reduction will result. The PDF for the sum of M uncorrelated ambiguity surfaces is found using moment generating functions:

$$P(b) = \mathcal{L}^{-1}\left(\prod_{n=1}^{M} \mathcal{L}(P_{NB}(b|f_n))\right), \tag{17}$$

where $\mathcal{L}$ denotes the Laplace transform. Using the transformed narrow-band distribution $\mathcal{L}(e^{-b/\mu}/\mu)=(1/\mu)[1/(s+1/\mu)]$ along with the definition of the inverse transform, the PDF for the averaged surface is found as

$$P_{BB}(b) = \frac{M}{2\pi i}\int_{\gamma-i\infty}^{\gamma+i\infty} \left(\prod_{n=1}^{M} \frac{1}{\mu_n}\right)\left(\prod_{n=1}^{M} \frac{1}{s+1/\mu_n}\right) e^{sbM}\, ds, \tag{18}$$

where the factors of M in the leading fraction and the exponent account for the number of frequencies being averaged. The narrow-band terms μ_n will vary with frequency and will be unique. The integral above can then be solved as a contour integration with each frequency giving rise to a simple pole in the complex plane. Summing the residues of these poles gives the final result:

$$P_{BB}(b) = M\left(\prod_{n=1}^{M} \frac{1}{\mu_n}\right)\sum_{n=1}^{M}\left(\prod_{m=1,m\neq n}^{M} \frac{\mu_m\mu_n}{\mu_n-\mu_m}\right) e^{-bM/\mu_m}. \tag{19}$$

Although the narrow-band coefficients μ_n are unique, they often vary slowly with frequency. This can give rise to numerical instabilities. If the μ_n are approximated as constant, the broadband distribution is a central χ^2 distribution with $2M$ degrees of freedom:

$$P_{BB}(b) = \frac{M}{\sigma_Y^{2M} 2^M \Gamma(M)} (bM)^{M-1} e^{-bM/2\sigma_Y^2}, \tag{20}$$

or, in terms of μ,

$$P_{BB}(b) = \frac{M}{\mu^M \Gamma(M)} (bM)^{M-1} e^{-bM/\mu}. \tag{21}$$

The higher-order χ^2 distributions are characterized by a reduced probability of either very large or very small values. Frequency averaging fills in the troughs of the sidelobes in addition to averaging down the peaks. The *average* peak to sidelobe ratio for this form of incoherent averaging is μ, the same as for narrow-band processing, but the shape of the distribution is different.

The derivation above assumes that the sidelobe locations are uncorrelated across frequency. Waveguide invariant arguments can be used to estimate the frequency spacing required for this to be true.[12,15] The migration of CMFP sidelobes with frequency is described by

$$\frac{\delta\omega}{\delta r} = \beta\frac{\omega}{r-R}, \tag{22}$$

where R is the true range to the source and β is the waveguide invariant. β is roughly 1 for many shallow water scenarios. For the CMFP sidelobes to shift by one CMFP range main lobe L_r, a frequency shift of

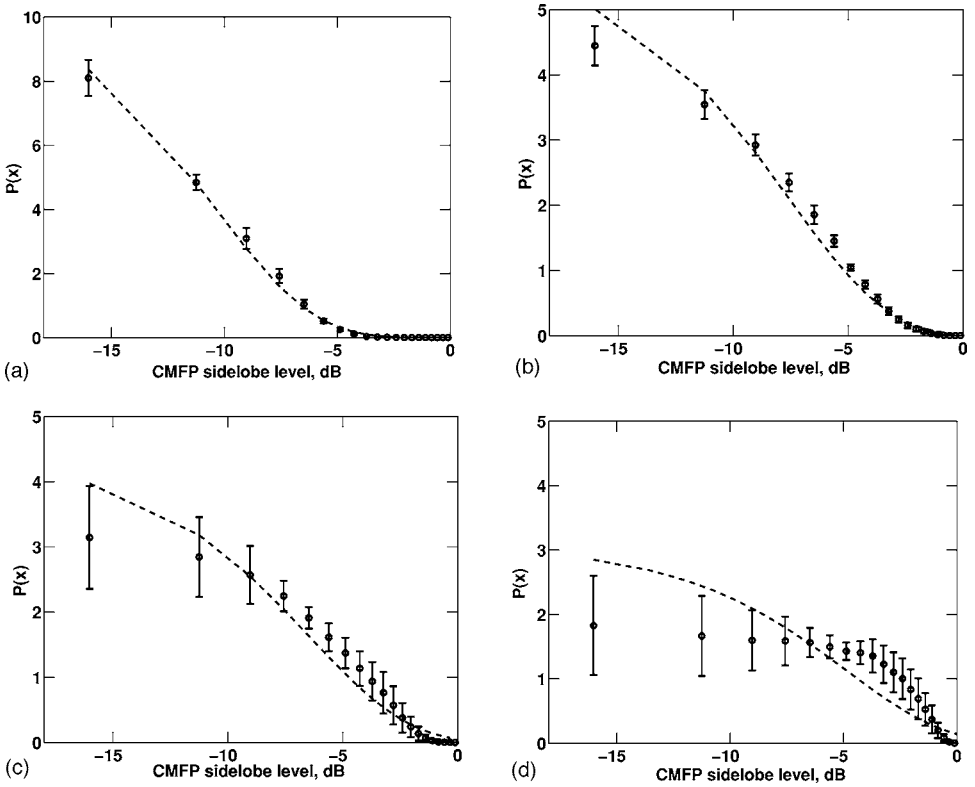

FIG. 4. Comparison of predicted PDFs (dashed lines) with distributions estimated from Monte Carlo runs. Histograms were generated for individual Monte Carlo runs and used to produce the averaged distribution ± one standard deviation. Agreement is close for the 80% spanning VLA and degrades as effective vertical aperture is reduced.

$$\Delta f \geqslant \frac{fL_r}{r-R} \tag{23}$$

is required. The main lobe size in range is given by $L_r = 2\pi/(k_1 - k_N)$.[10] Since sidelobes shift faster with increasing distance from the source, frequency averaging reduces MFP levels away from the source more rapidly. Setting $r-R = 1$ km in Eq. (23) suggests, for the scenarios considered below, a frequency spacing of roughly 10 Hz. Adding frequencies at a finer spacing is not expected to help reduce ambiguities in the MFP output.

VI. NUMERICAL RESULTS

Simulations were carried out to test the results above. CMFP power was simulated for an ensemble of random source ranges and depths. The output power from these surfaces was used to generate histograms which were normalized to estimate PDFs. A mean distribution and standard deviations around it were calculated and are compared to the predicted distribution.

Figure 4 shows a comparison of simulated and predicted distributions for narrow-band CMFP. For these cases, the source and look direction depths and ranges were allowed to vary uniformly over the MFP search grid shown in Fig. 2. For the 80% spanning VLA the agreement to the overall shape is quite good. Of the arrays considered, this one best satisfies the assumption used to derive the approximate normalization in Eq. (8).

The match between predictions and simulation degrades for the less capable arrays. As discussed above, one possible metric for the accuracy of Eq. (13) is the probability of nonphysical outputs $[\Pr(b>1)]$. This probability is calculated to be 1.1e-5 for the 80% spanning VLA, 0.003 for the 40% spanning VLAs, 0.0094 for the 1 km HLA, and 0.046 for the 500 m HLA. Reasonable matches to the analytic model are seen for cases where $\Pr(b>1)<0.01$. It is worth noting that the relevant parameter for mode cross-talk is the array length in wavelengths. Thus the agreement for the 500-m array at 240 Hz should be comparable to the agreement seen for the 1-km-long array at 120 Hz.

The simulations in Fig. 2 showed that the HLA apertures could provide some discrimination between surface and submerged depth zones. The ability of the analytic results to predict this is tested by restricting the look directions D_{l1} and D_{l2} in the calculation. A comparison between calculated and simulated results is shown in Fig. 5 for the 1-km-long HLA example. The "surface" depth zone is defined as 0–20 m, with the "submerged" zone defined as the rest of the water column. The analytic prediction is successful in predicting the surface/submerged trends in output power distribution.

Simulations are next used to examine the output distribution for incoherent broadband MFP. The analysis above showed that a simplification is possible if the narrow-band variances are fairly flat with frequency. These variances were examined and found to vary by less than 10% over the frequency range considered. cases considered. Thus Eq. (21), which assumes constant variance with frequency, was used for the calculation.

Figure 6 shows a comparison of the predicted and simulated distributions for incoherent broadband MFP. The calcu-

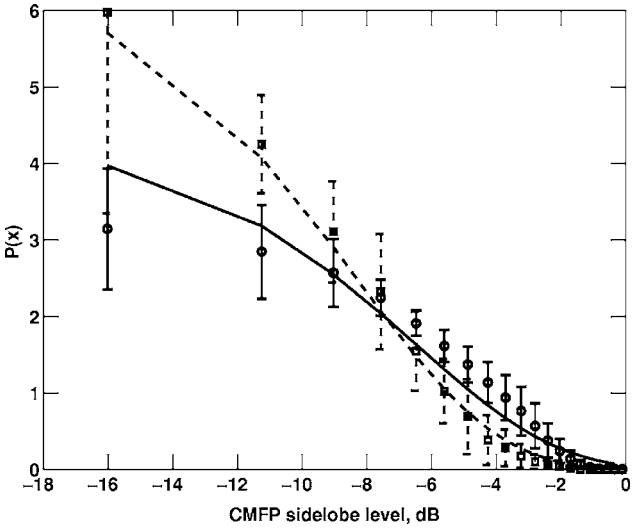

FIG. 5. Predicted PDF for depth zones [1–20 m] and [20–209 m] compared to Monte Carlo results, 1 km HLA. Predictions are shown with lines, while Monte Carlo results are shown with error bars. Near-surface zone results are shown as dashed lines, while submerged zone results are solid. Note improved agreement between the model and Monte Carlo for the near-surface zone due to improved sampling of the high-order modes.

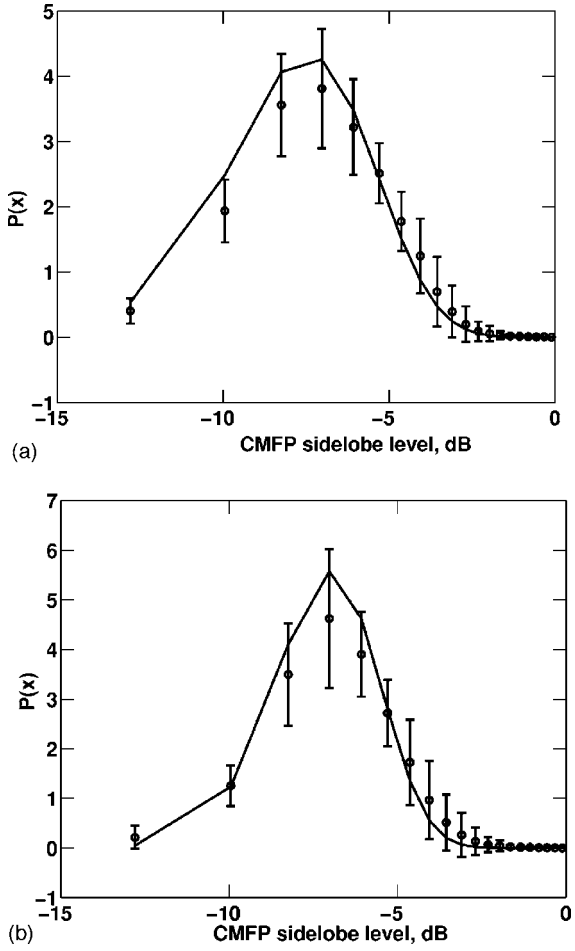

FIG. 6. Comparison of predicted PDFs for incoherent broadband averaging with distribution estimated from Monte Carlo runs. Predictions are shown with dashed lines, while Monte Carlo results are shown with error bars.

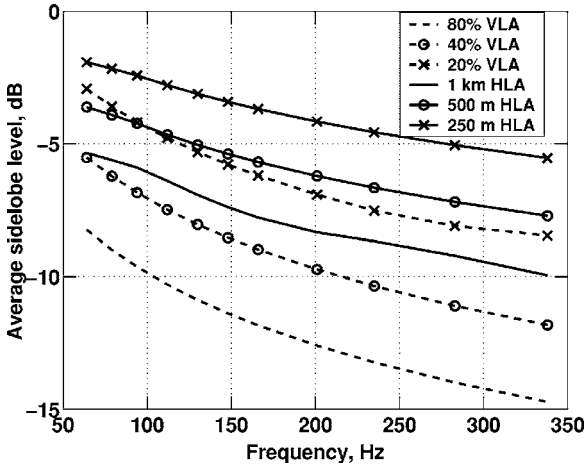

FIG. 7. Average sidelobe level (μ parameter) for narrow-band CMFP versus frequency and array geometry. The improved resolution and increased number of modes at high frequencies act to reduce average sidelobe levels. For HLAs, the sidelobe levels calculated are for the source bearing (endfire) only; lower sidelobes are present on other bearings.

lations were done for the 1-km-long HLA for bandwidths of 20 and 40 Hz. As the bandwidth increases, the distribution becomes more peaked; both high sidelobes and deep nulls in the frequency-averaged output become less likely. It is interesting to note that the agreement between the predicted and simulated distributions is closer than it was in the narrow-band case. This is presumably because variations in the steering vector normalization average out over frequency, making the approximation in Eq. (8) more accurate.

VII. SIDELOBE LEVELS VERSUS APERTURE AND FREQUENCY

The numerical results above have helped to validate the analytic results derived. In this section the analytic results are used to compare performance of several arrays versus frequency. The derived mean sidelobe level μ is also compared to a metric measuring MCM diagonality for use as a predictor of array performance.

Figure 7 shows the average sidelobe ratio calculated for single-frequency CMFP. This ratio is given by the parameter μ from Eq. (13), assuming that source power is normalized to one. The ratio is calculated for a set of tones in the range 64–338 Hz that correspond to projected tones used in SBCX. For HLAs, the results shown are for the endfire beam only. Results are shown for the four arrays discussed above and for two shorter arrays: a 250-m-long HLA (101 phones at 2.5-m spacing) and a 20% spanning bottom-mounted VLA. A trend is seen toward lower sidelobe levels at higher frequencies, where more modes can be coherently summed to reduce ambiguities.

As discussed above, a useful criteria for quantitative accuracy of the predictions is that the probability of nonphysical results be less than some threshold. Discussion following Fig. 4 suggested a criteria of $\Pr(b>1)<0.01$, which corresponds to an average sidelobe level of −6.6 dB or less. A less restrictive criteria of $\Pr(b>1)<0.05$ would suggest reasonable agreement for arrays with average sidelobe level of −4.76 dB or lower.

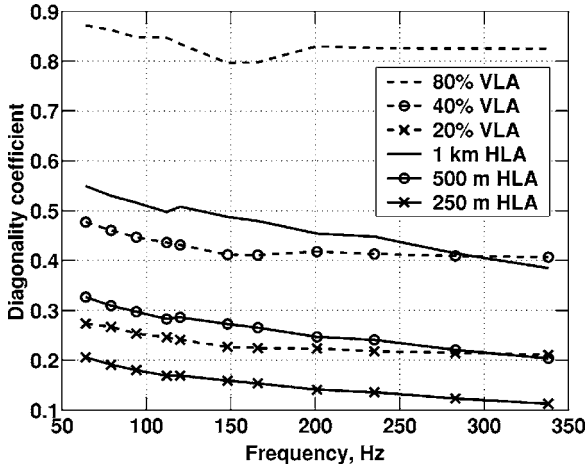

FIG. 8. Diagonality coefficient calculated for mode correlation matrices (MCMs); more diagonal is better. This metric roughly tracks the relative performance of the different arrays, but does not account for the different structure of VLA and HLA MCMs.

Previous studies have used metrics describing the diagonality of the mode correlation matrix (MCM) to compare arrays. The importance of the mode correlation matrix was discussed above. One problem with using a diagonality metric is that the structure of the MCM is not captured.

The MCM can be described using the following metric, which compares the power in the matrix diagonal to the power in all matrix elements:

$$d = \frac{|\mathrm{diag}(\mathbf{E})|^2}{|\mathbf{E}|^2_{\mathrm{frob}}}, \tag{24}$$

where $\mathbf{E}$ is the MCM and "frob" indicates the Frobenius norm.

Figure 8 shows this metric for the arrays and frequency ranges shown above. This metric gives a ranking which is similar to that seen in Fig. 7, but some noticeable differences exist. The diagonality coefficient shows the 1-km HLA and 40% VLA as being extremely similar, with the 1-km HLA having a slightly more diagonal MCM. Figures 7 and 2 both show the 1-km HLA as having slightly *worse* performance, in spite of its higher diagonality. The explanation is that the MCM metric does not capture the MCM structure for HLAs, which typically have worse resolution for the low-order modes that can dominate submerged source response. In contrast, Eq. (13) weights the MCM values by factors that account for mode excitation and attenuation, leading to improved qualitative agreement with direct numerical ranking of array performance.

VIII. SUMMARY

This article has addressed the prediction of sidelobe levels for conventional matched field processing. An approach was developed for analytically predicting the distribution of output power in conventional MFP ambiguity surfaces as a function of array aperture and processing bandwidth. These investigations are intended to provide tools for MFP array design that complement the use of numerical simulations and array design trade studies.

ACKNOWLEDGMENTS

The author would like to thank his co-workers Nigel Lee, Lisa Zurk, Jennifer Watson, and Bill Payne for helpful discussions on this topic. Suggestions and comments made by Dr. Samuel Earp and the reviewers are also gratefully acknowledged. This work was sponsored by DARPA-ATO under Air Force Contract No. F19628-00-C-0002. Opinions, interpretations, conclusions, and recommendations are those of the author and are not necessarily endorsed by the United States Government.

APPENDIX: VARIANCE CALCULATION

In this appendix the variance of the Y_{mn} terms shown in Eq. (8) is calculated. This variance is used to calculate the parameter μ describing the exponential distribution for narrow-band CMFP.

To review, the quantities in the CMFP power output which are randomly varying under the assumptions listed in Sec. IV are collected into the term

$$Y_{nm} = \frac{2\pi}{\sqrt{k_n k_m}} \frac{\psi_n(z_s)\psi_m(z) e^{i(k_n r_s - k_m^* r)}}{|\mathbf{p}_{\mathrm{look}}(\Theta)||\mathbf{x}(\Theta_S)|}. \tag{A1}$$

The exponential terms in the random quantity Y_{nm} can be rewritten as

$$e^{i(k_n r_s - k_m^* r)} = e^{i\phi} e^{-\alpha_m r} e^{-\alpha_n r_s}. \tag{A2}$$

The phase associated with the random source and look direction ranges has been collected into a phase term $e^{i\phi}$. Although this phase actually depends on r and r_s, treating it separately separates out the very rapid fluctuation in phase from the much slower change in attenuation. Y_{nm} is a complex zero-mean random variable. Since the argument to the exponential can range over $0-2\pi$, the real and imaginary parts have equal variance, given by

$$\sigma^2_{nm} = \frac{4\pi^2}{k_n k_m} \int \frac{\psi_m^2(z)\psi_n^2(z_s)}{|\mathbf{p}_{\mathrm{look}}(\Theta)|^2 |\mathbf{x}(\Theta_S)|^2} \times \cos^2[\phi(r)] e^{-2\alpha_n r_s} e^{-2\alpha_m r} p_{\mathbf{r}}(\mathbf{r})\, d\mathbf{r} \tag{A3}$$

with $\mathbf{r}$ representing the independent random variables r_s, z_s, r, z, and ϕ, and $p_{\mathbf{r}}(\mathbf{r})$ representing their probability density function. The $\cos^2[\phi(r)]$ term comes from the real part of the complex exponential. A similar equation containing a $\sin^2[\phi(r)]$ term is obtained for the variance of the imaginary part. These terms both average to $\frac{1}{2}$, giving the result quoted in Sec. IV.

The normalization of the pressure fields is required next. For an array that resolves the modes well, off-diagonals will not contribute strongly to the intensity, and the norm-squared for the look direction vector is

$$|\mathbf{p}(\Theta)|^2 \approx \sum_l \frac{2\pi}{k_l} \psi_l^2(z) e_{ll} e^{-2\alpha_l r}. \tag{A4}$$

Attenuation acts to eliminate contributions from high angle modes, so almost all the contribution at longer ranges is from the trapped or "proper" modes. This allows a further simplification:

$$|\mathbf{p}(r,z)|^2 \approx \sum_{l=1}^{N_p} \frac{2\pi}{k_l} \psi_l^2(z) e_{ll} e^{-2\alpha_l r_{\text{mid}}}, \tag{A5}$$

where r_{mid} is the mid-range of the MFP search region whose statistics are being studied. Numerical tests indicated that this further simplification did not introduce errors for the cases studied.

Next, the approximation in Eq. (A5) is substituted into Eq. (A4). Because the source location and look directions are independent random variables, integration over these variables can be done separately:

$$\begin{aligned}\sigma_{nm}^2 = \frac{4\pi^2}{k_n k_m} & \left[\frac{1}{\Delta_{Dl}} \int_{D_{l1}}^{D_{l2}} dz \, \frac{\psi_m^2(z)}{\sum_{l=1}^{N_p} (a/k_l) \psi_l^2(z) e_{ll} e^{-2\alpha_l r_{\text{mid}}}} \right] \\ & \times \left[\frac{1}{\Delta_{Ds}} \int_{D_{s1}}^{D_{s2}} dz_s \, \frac{\psi_n^2(z_s)}{\sum_{p=1}^{N_p} (a/k_p) \psi_p^2(z_s) e_{pp} e^{-2\alpha_p r_{\text{mid}}}} \right] \\ & \times \left[\frac{1}{\Delta R} \int_{R}^{R+\Delta R} dr \, e^{-2\alpha_m r} \right] \\ & \times \left[\frac{1}{\Delta R} \int_{R}^{R+\Delta R} dr_s \, e^{-2\alpha_n r_s} \right]. \end{aligned} \tag{A6}$$

The first two terms in brackets are the Z_m terms from Sec. IV, while the two range integrals can be evaluated to give the R_m terms. The equation above then gives the result quoted in Eq. (10).

[1] W. Burdic, *Underwater Acoustic Systems Analysis*, 2nd ed., (Prentice-Hall, Englewood Cliffs, NJ, 1991).

[2] A. Baggeroer, W. Kuperman, and P. Mikhalevsky, "An overview of matched field methods of ocean acoustics," IEEE J. Ocean. Eng. **18**(4), 401–424 (1993).

[3] H. C. Song, "Performance bounds on the passive localization of a moving source for ocean acoustics," Ph.D. thesis, Massachusetts Institute of Technology, September 1990.

[4] J. Buck, J. Preisig, and K. Wage, "A unified framework for mode filtering and the maximum a posteriori mode filter," J. Acoust. Soc. Am. **103**, 1813–1824 (1998).

[5] V. Premus, "Mode scintillation index: a physics-based statistic for acoustic source depth discrimination," J. Acoust. Soc. Am. **105**, 2170–2180 (1999).

[6] A. Baggeroer and H. Cox, "Passive sonar limits upon nulling multiple moving ships with large aperture arrays," 33rd Asilomar Conference on Signals, Systems and Computers, pp. 103–108 (1999).

[7] C. Bogart and T. C. Yang, "Source localization with horizontal arrays in shallow water: Spatial sampling and effective aperture," J. Acoust. Soc. Am. **96**, 1677–1686 (1994).

[8] S. Tantum and L. Nolte, "On array design for matched-field processing," J. Acoust. Soc. Am. **107**, 2101–2111 (2000).

[9] G. Smith, C. Feuillade., and D. DelBalzo, "Matched-field processing enhancement in a shallow-water environment by incoherent broadband averaging," J. Acoust. Soc. Am. **91**, 1447–1454 (1992).

[10] L. Zurk, N. Lee, and J. Ward, "Source motion mitigation for adaptive matched field processing," J. Acoust. Soc. Am. **113**, 2719–2731 (2003).

[11] M. Porter, "The KRAKEN normal mode program," SACLANT Undersea Research Centre Technical Report SM–245, 1991.

[12] R. Brienzo and W. Hodgkiss, "Broadband matched-field processing," J. Acoust. Soc. Am. **94**, 2821–2831 (1993).

[13] E. Westwood, "Broadband matched-field source localization," J. Acoust. Soc. Am. **91**, 2777–2789 (1992).

[14] A. Baggeroer, W. Kuperman, and H. Schmidt, "Matched field processing: Source localization in correlated noise as an optimum parameter estimation problem," J. Acoust. Soc. Am. **83**, 571–587 (1988).

[15] A. Thode, W. Kuperman, G. D'Spain, and W. Hodgkiss, "Localization using Bartlett matched-field processor sidelobes," J. Acoust. Soc. Am. **107**, 278–286 (1990).